



SmartLens : Sensing Eye Activities Using Zero-power Contact Lens

Liyao Li^{*★}, Yaxiong Xie[†], Jie Xiong[‡], Ziyu Hou^{*★}, Yingchun Zhang^{*★},
Qing We^{*★}, Fuwei Wang^{*★}, Dingyi Fang^{*★}, Xiaojiang Chen^{*★△}

^{*}Northwest University (China), [†] University at Buffalo SUNY, [‡] University of Massachusetts Amherst,

^{*} Shaanxi International Joint Research Centre for the Battery-Free Internet of Things

^{*}{liiyao, houziyu1, zhangyingchun, weiqing}@stumail.nwu.edu.cn,

[†]yaxiongx@buffalo.edu, [‡]jxiong@cs.umass.edu, ^{*}{wfw, dyf, xjchen}@nwu.edu.cn

ABSTRACT

As the most important organs of sense, human eyes perceive 80% information from our surroundings. Eyeball movement is closely related to our brain health condition. Eyeball movement and eye blink are also widely used as an efficient human-computer interaction scheme for paralyzed individuals to communicate with others. Traditional methods mainly use intrusive EOG sensors or cameras to capture eye activity information. In this work, we propose a system named SmartLens to achieve eye activity sensing using zero-power contact lens. To make it happen, we develop dedicated antenna design which can be fitted in an extremely small space and still work efficiently to reach a working distance more than 1 m. To accurately track eye movements in the presence of strong self-interference, we employ another tag to track the user's head movement and cancel it out to support sensing a walking or moving user. Comprehensive experiments demonstrate the effectiveness of the proposed system. At a distance of 1.4 m, the proposed system can achieve an average accuracy of detecting the basic eye movement and blink at 89.63% and 82%, respectively.

CCS CONCEPTS

• Hardware → Wireless devices; • Human-centered computing → Ubiquitous and mobile computing systems and tools;

KEYWORDS

Contact lens, Backscatter, Eye movement sensing, Battery-free, Wireless, Low cost, IOT

ACM Reference Format:

Liyao Li^{*★}, Yaxiong Xie[†], Jie Xiong[‡], Ziyu Hou^{*★}, Yingchun Zhang^{*★},
Qing We^{*★}, Fuwei Wang^{*★}, Dingyi Fang^{*★}, Xiaojiang Chen^{*★△}. 2022.
SmartLens : Sensing Eye Activities Using Zero-power Contact Lens. In *Proceedings of The 28th Annual International Conference On Mobile Computing And Networking (ACM MobiCom '22)*. ACM, Sydney, NSW, Australia,
14 pages. <https://doi.org/10.1145/3495243.3560532>

△ Corresponding author.

Permission to make digital or hard copies of all or part of this work for personal or classroom use is granted without fee provided that copies are not made or distributed for profit or commercial advantage and that copies bear this notice and the full citation on the first page. Copyrights for components of this work owned by others than ACM must be honored. Abstracting with credit is permitted. To copy otherwise, or republish, to post on servers or to redistribute to lists, requires prior specific permission and/or a fee. Request permissions from permissions@acm.org.

ACM MobiCom '22, October 17–21, 2022

© 2022 Association for Computing Machinery.

ACM ISBN 978-1-4503-9181-8/22/10...\$15.00

<https://doi.org/10.1145/3495243.3560532>

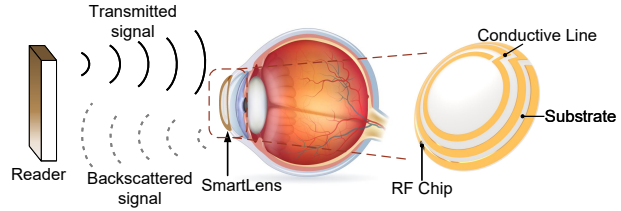


Figure 1: A tag embedded inside the contact lens harvests energy from the RF signal and backscatters signals back to the reader.

1 INTRODUCTION

Human eyes are one of the primary tools for humans to gather information about their surroundings. There are numerous neurons between the brain and the eyes that deliver the rich information captured by the eyes. Therefore, eye movement patterns indicate brain health condition, so it can be used to aid early diagnosis of nervous system diseases, such as ADHD [16, 37], autism [12, 36], Parkinson's disease [32], Alzheimer's disease [14], and depression [5]. Prior works [7, 51] also leverage eye movements to effectively determine the driver's fatigue status and provide timely alarms to the driver to prevent car accidents. Furthermore, eye movement data can also be used as a human-computer interaction method [20] to support applications such as message typing for paralyzed individuals [40, 41], and meta/virtual reality [11, 29]. The aforementioned applications motivate a cost-effective and non-operative system that can continuously monitor the user's eye movement state.

Existing works have proposed a variety of methods for eye movement detection, which can be broadly classified into two groups, i.e., contact-based [23, 25, 39, 47] and non-contact based [28]. Contact based methods require attaching hardware to the human skin. For example, the multi-channel EOG electrodes, which achieve high-precision eye movement tracking but are invasive. To make the EOG measurement less invasive, prior works propose to integrate the EOG sensor into headsets or glasses [25, 47], which, however, significantly reduces the accuracy since the EOG sensors are very sensitive to the number of channels and the location of the attachment. The headsets or glasses provide limited sensing channels and cannot place the sensor at optimal locations. Non-contact methods primarily rely on cameras to capture eye movements, which can provide high-precision eye tracking. However, changes in illumination will reduce the tracking accuracy, and camera-based solutions also raise privacy concerns.

In this paper, we propose SmartLens, a low-cost and battery-free eye movement sensing system. SmartLens is a backscatter

tag consisting of a commercial chip and a customized antenna embedded into the contact lens, as shown in Figure 1. The tag harvests energy from the RF signal to power itself and backscatters the modulated information to the reader. Any eye-related activities, such as eye blinks or rotation of the eyeball, would significantly affect the backscattered signal since the contact lens directly cover the human eyes. Therefore, SmartLens recognizes eye blinks and eye movement by analyzing the variations in the backscattered signals. SmartLens leverages RF signals to sense eye activities and is thus immune to the illumination condition. Compared with other contact-based methods, SmartLens provides better user experience since the human is only required to wear a contact lens, which is much more lightweight than the multichannel EOG sensor or the headset and glasses with embedded EOG sensor.

To realize our idea into a practical system, we face two major challenges. First, we need to design a backscatter tag that has similar size as contact lens and at the same time supports meter-level communication range. To further complicate matters, the nontransparent backscatter tag can only cover a ring area within the lens to prevent blockage of the human view. The size of the tag forces us to adopt a complicated and compact antenna design, *i.e.*, a circular dipole antenna with multiple loops, just as shown in Figure 1. The closely placed conductive line introduces serious mutual coupling effect, so any subtle modifications to the antenna structure, *e.g.*, changing the width of the loop, the space between loops, or the length of the antenna, would significantly affect the impedance and thus the efficiency of the antenna.

To simultaneously meet the rigorous size and communication range requirement, we develop a multistage antenna design workflow that handles the mutual coupling between antenna loops, impact of the human tissue, influence of the 3D structure of the antenna and the engineering deviation during the tag fabrication. Specifically, we first build an accurate antenna model to understand the mutual coupling and the impact of human tissue, based on which we solve the impedance matching equation to obtain the initial antenna structural parameters. We then iteratively refine our antenna design using the software simulation to include the impact of the 3D structure and at the same time mitigate the impact of engineering deviation.

The second challenge stems from interference. SmartLens senses eye blink or eyeball rotation by analyzing the signal variations induced by those eye related activities. But there are some significant number of interference sources that also introduce variations to the backscattered signals, such as head movement, hand movement, sitting and jumping. To mitigate the impact of interference, we propose attaching a reference tag to the head. The reference tag and the tag inside the contact lens are static to each other, even when the human is moving. Therefore, SmartLens leverages the variations in the difference of signals collected from the reference tag and the tag in the lens to sense the eye movement.

We built a prototype SmartLens contact lens by laser engraving the conductive layer to fabricate the antenna, connecting the antenna to the chip, and then embedding the whole tag in polydimethylsiloxane (PDMS), a widely used material for contact lens.¹

¹The design of SmartLens is available at: <https://github.com/Nisl-lly/Smartlens>.

We evaluate the performance of SmartLens in a variety of usage scenarios with a commercial R420 reader serving as the transceiver. Extensive real-world indoor environment results demonstrate that SmartLens achieves long-range, accurate and robust eye movement detection. Specifically, SmartLens's detection range is **1.5 m** and **1.1 m**, when we attach the contact lens to bionic eyes and the eyes of a dead pig (all of our experiments are approved by the IRB of our university). The average accuracy of detecting the basic eye movement and blink is 89.63% and 82% when the distance between the tag and the reader is 1.4 m. SmartLens is also immune to interference from other activities of the same human or other human in the same propagation environment.

Contributions. We present a passive RF tag embedded inside contact lens that can be worn on the eyes and detect eye movement. SmartLens is the first system to apply UHF RF signals for eye movement detection. Through hardware design, we have increased the communication range from 0.3 m (first design) to 1.5 m (current design). Through theoretical and experimental analysis, we model the phase changes caused by eye movement. We address the impact of the environment and human motions on eye movement detection. Finally, we put the SmartLens on a real pig's eye and assess the communication distance.

2 RELATED WORK

In this section, we discuss the work related to eye movement detection, RFID sensing, and contact lens sensing.

Eye movement detection. Existing eye-movement detection systems can be mainly grouped into two categories, *i.e.*, contact based and non-contact based.

(i) *Non-contact based:* The image based non-contact eye sensing methods [15, 26] leverage cameras to capture the pictures or videos of eyes and then detect the eye movement via image processing methods and machine learning techniques. Such methods achieve high accuracy in identifying blinks and measuring the angle of the eyeball rotation, but suffer from poor lighting conditions and raise concerns of possible privacy leakage. The acoustic based eye sensing method [28] detects eye blinks by analyzing the signal variations caused by blinks, which, however, cannot detect finer-grained eye ball movement such as rotation.

(ii) *Contact-based:* The contact-based method uses EOG electrodes, a special sensor embedded in the eye patch [17], helmet [24], and glasses [53] for eye movement detection. Eye movement detection with EOG electrodes is accomplished by touching the electrodes to the skin to detect eye movements by tracking the EOG signal changes. The measured signal may be interfered with and distorted by other body movements, and hence it is necessary to build multi-stage filter-amplifiers at the receiving side to obtain an accurate signal, resulting in significant complexity in hardware design. SmartLens implements a lightweight customized lens embedded with small and battery-free RFID tags, significantly improving the user experience compared with the invasive EOG electrodes.

RFID sensing. In recent years, RFID-based sensing has garnered considerable attention. Diverse applications have been proposed, ranging from detecting vibrations with the sub-millimeter resolution [50] to monitor the vital signals such as breathing [8, 46, 54] and heartbeat [33, 55]. Typically, these methods employ tag arrays

which are capable of enhancing the target signal while suppressing interfering signals by fusing RF signals from multiple tags. In addition, due to the large size of commercial tags, they lose their significance for detecting eye movements or fine-grained perception in limited scenes.

Contact lens based sensing. Embedding vital sensors, e.g., glucose sensor, into contact lens to monitor vital signals, such as the blood sugar level [1, 9, 21, 22, 27, 30] has recently attracted significant attention. Depending on the signal used to power the sensors and read the measured sensing data, the contact lens based sensing system can be categorized into two types: the magnetic field based and the RF signal based.

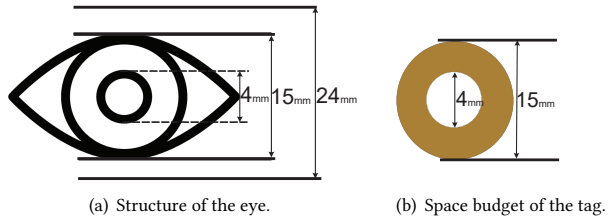
For magnetic field based design, both the reader and the contact lens are equipped with coil antennas. The reader delivers the energy to the contact lens via inductive coupling between coils. The variations in vital signals affect the impedance of the glucose sensor and thus change the coupling effects between two coils. Hence, the reader reads the sensed vital signal by monitoring the variations in the coupling effects. We, however, note that because of the limited coil size at the contact lens, the communication range is limited to approximative 10 cm. Besides, according to the inductive coupling theory, any slight misalignment between coils of the reader and the contact lens could significantly jeopardize the energy harvesting and data transmission performance, which restricts its usability.

RF based solutions [1, 9, 21] leverage electromagnetic wave to power the integrated circuits embedded inside the contact lens. Similar to a standard RFID system, the reader reads the measured sensor data via backscatter communication. Most of the prior works [9, 21] focus on designing the circuits and use a simple circular antenna for power harvesting and backscattering. Due to the limited size of the simple antenna and the severe signal blockage caused by the human tissue, such solutions only support a communication range of 1 cm to 2 cm. Google contact lens [1] is another famous RF-based contact lens sensing system that uses a multi-loop antenna to detect blood glucose through the tears. We note that there is no public technical documentation of the implementation and the performance of Google contact lens. Also, a recent work [21] points out that Google contact lens has a Li battery in its design and thus is not battery-free. SmartLens also relies on RF signal to power the circuits, but significantly improves the sensing range to more than one meter, with a carefully designed spiral tiny loop dipole antenna. SmartLens is purely battery-free, and its circuit and antenna design are open-source [4].

Contact lens based display. Using the contact lens as a screen to display diverse information has huge potential for augmented reality. Recent works [27, 30] design RF signal powered contact lens based display that supports only a single LED pixel. The RF-based display has strict requirement on the distance, i.e., less than 10 cm between the RF signal emitter (power source) and the contact lens display, which significantly affects the user experience. Mojo [3] and inWith [2] are two commercial contact lens that support imaging processing and display processed information, which, however, require on-lens battery and thus frequent battery re-charging.

3 HARDWARE DESIGN OF SMARTLENS

We begin this section by presenting the overview of SmartLens (§ 3.1). We then describe the design of the overall structure of the SmartLens



(a) Structure of the eye. (b) Space budget of the tag.

Figure 2: The structure of human eyes determines the space budget of the SmartLens tag. The average diameter of Pupils is typically 2 – 4 mm [44], and the diameter of contact lenses is no larger than 15 mm [49]. The average diameter of adult eyes is 24 mm [6].

antenna (§ 3.2), which is further fined tuned to maximize the sensing and communication performance (§ 3.3). Finally, we introduce the fabrication process (§ 3.4) of the SmartLens tag.

3.1 Overview

In this section, we introduce the overall system architecture of SmartLens and list the performance goal that we need to achieve when designing the hardware.

3.1.1 System architecture. SmartLens relies on signal backscatter for simultaneous communication and sensing. A reader that sends the wireless signal to query the status of eyes, just as shown in Figure 1. The tag inside the contact lens receives the signal to power itself and also backscatters the query signal to the reader. By analyzing the backscattered signal, the reader is able to detect the eye movement. We focus on designing the hardware of the backscatter tag inside the contact lens in this section and present the signal processing algorithm in Section § 4.

3.1.2 Performance goal of SmartLens. In this section, we describe the two design goals of the tag hardware design.

User experience. The hardware of SmartLens is a special version of contact lens and will be worn by a human for a long time, so it is crucial for us to optimize the user experience. There are two factors that greatly affect the user experience of SmartLens. First of all, the view blockage of the hardware, including both the antenna and chip. The light goes into the eyes via the pupil so any blockage to the pupil affects the view of the human. Our tag must provide a clear path for the light that goes into the pupil and should locate outside of the pupil, just as shown in Figure 2 (a). We embed our tag into the contact lens so its size is also limited by the size of the lens. As a result, the space budget of our tag is lower bounded by the size of the pupil and upper bounded by the size of the contact lens, just as shown in Figure 2 (b). The second factor is the 3D structure of the tag antenna. To make people feel comfortable wearing the tag, we need to curve the antenna in 3D space to match the shape of the eyeballs. Both the space budget and the 3D structure of the tag affect the design of the tag hardware.

Communication and sensing range. The communication and sensing range is a key performance metric which depends on the operating frequency and the antenna design. Generally speaking, the antenna size of high frequency signals can be small which fits our space budget well. Signals with higher frequency, however, have higher loss in the tear as well as in the human body tissue. Signals with lower frequency have better penetration over human tissue

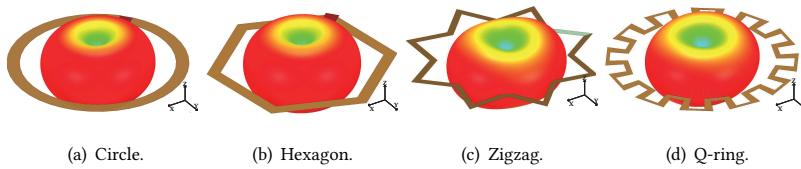


Figure 3: The radiation pattern of various shaped antennas. (The impedance of the chip: (30.53-211.81j)).

but require longer antenna for efficient signal reception. To balance the efficiency and space budget, we choose sub-GHz band as our operating frequency. The design of the tag antenna significantly affects the backscattering efficiency and thus the sensing range, which we will introduce in detail in the rest of this section.

3.2 Antenna Design

We consider two important performance metrics of the antenna that contribute most to the communication range, i.e., the *voltage standing wave ratio* (VSWR) and the radiation pattern.

VSWR. The VSWR measures the ratio of the power not radiated (and thus wasted) by the antenna to the total power delivered to the antenna, which is given by:

$$VSWR = \frac{1 + |\Gamma|}{1 - |\Gamma|} = \frac{Z_a + Z_o + |Z_a - Z_o|}{Z_a + Z_o - |Z_a - Z_o|} \quad (1)$$

where Z_a and the Z_o are the impedance of the antenna and the characteristic impedance of the chip, respectively. Γ is the reflection coefficient at both end of the chip. According to the antenna theory, the ratio is minimized if $Z_a = Z_o$. We directly connect the antenna to a commercial RFID chip, just as shown in Figure 3, so we need to match the impedance of the antenna with the RFID chip. The impedance of the RFID chip in our design is $30.53 - 211.81j$, where 30.53 is the resistance and $-211.81j$ is the capacitance and inductance.

Radiation Pattern. The radiation pattern is the representation of the distribution of radiated energy into space, as a function of direction. When the electromagnetic waves reach the antenna, an induced current is excited on the surface of the antenna. The induced current can be viewed as consisting of multiple current elements, each current element forming a radiation field in space. The radiated pattern of the antenna mainly consists of the radiated fields produced by the current elements on the surface of the antenna.

3.2.1 The basic shape. We first determine the basic shape of our antenna and then fine-tune the detailed structure. Confined by the space budget, the overall shape of our tag antenna is similar to a ring as shown in Figure 2. To get a better sense of the performance of a ring style antenna, we use HFSS to estimate the impedance and radiation pattern of a circular ring, a hexagon ring, a zig-zag ring, and a Q-ring and plot the estimated results in Figure 3. Since all the radiation patterns of ring style antennas are similar to each other, we pick the simple circular antenna as the fundamental structure of our tag antenna. We also observe that the impedance of all the ring style antennas are way smaller than the RFID chip (30.53), motivating a further revision over the simple circular antenna.

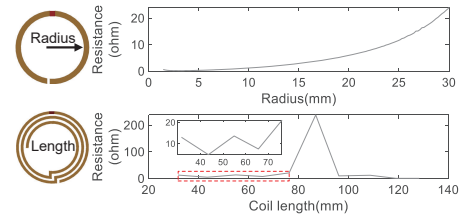


Figure 4: The resistance under different lengths and radius of the antenna loop.

3.2.2 Physical length of the antenna. The physical length of the antenna is a parameter that significantly affects the antenna's resistance, just as we have modeled in Section § 3.3. Generally, the longer the physical length, the larger the resistance, according to the transmission line theory. Therefore, to match the resistance of the chip, we need to increase the length of the tag antenna. On the other hand, a longer circular ring antenna may not fit the space budget. To balance the space budget and the physical length, we propose using circular antenna with multiple loops, just as shown in Figure 4. We note that, due to the mutual coupling between different loops, the resistance doesn't increase monotonically with the physical length. We need to fine-tune the detailed antenna structure to minimize the VSWR.

3.3 Fine-tuning the Antenna Structure

We fine-tune the structure of a circular antenna with multiple loops to match the impedance of the antenna and the chip. We first model the impact of the human eyes and the structural parameters of the antenna, e.g., the physical length of the antenna, the width of the conductive line and the space between loops, which influence the final impedance. We then solve the impedance matching equation to find the optimal antenna structure. At last, we propose an iterative refinement procedure to compensate for the offset between the theoretical model and the manufactured hardware.

3.3.1 SmartLens antenna model. The antenna is a resonator, whose impedance can be represented as:

$$\begin{aligned} Z_a &= Z_r + Z_i + Z_c \\ &= R + j\omega L + \frac{1}{j\omega C} \end{aligned} \quad (2)$$

where $Z_r = R$ is the resistance, $Z_i = j\omega L$ is the inductance and the $Z_c = \frac{1}{j\omega C}$ is the capacitance of the antenna. ω is the angular frequency which can be calculated by $2\pi f$, where f is the operating frequency of the antenna. The impedance of the antenna is affected by four factors, i.e., the human eyes, structural parameters of the antenna, material of the substrate and conductive layer, and the curving of the antenna to fit the human eyes.

Impact of human eyes and structural parameters. We theoretically model the impact of the human eyes and the structural parameters on the impedance of the antenna. We model the capacitance, resistance, and inductance separately.

Capacitance. The capacitance of our tag antenna is affected by the tissue of human eyes, the tears and the structure of the antenna. To derive the overall capacitance, we first model the capacitance introduced by the antenna and then extend the model to include the impact of eyes and tears.

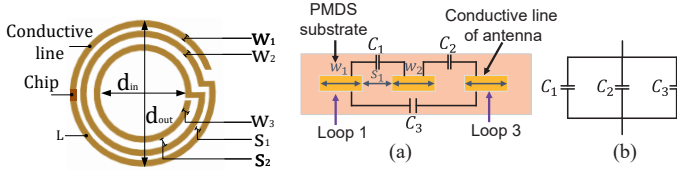


Figure 5: The structure of tag antenna.

We illustrate our model using an example of a circular antenna with three loops, as shown in Figure 6. Every two conductive lines form a capacitor whose capacitance can be calculated as:

$$C = \frac{\epsilon_r l \ln \left(2 \frac{(1 + \sqrt{1 - k^2})}{(1 - \sqrt{1 - k^2})} \right)}{377\pi v_0} \quad (3)$$

where ϵ_r is the *permittivity* of the substrate medium and v_0 is a constant representing the *phase velocity* of light propagation in free space, which can be calculated using the permeability of free space and permittivity of air [31]. l is the length of the conductive line. The parameter k is given by $k = \frac{s}{s+w_1+w_2}$, where s is the gap between two conductive lines, and w_i ($i = 1, 2$) is the width of the conductive lines. According to the above analysis, we see that one circular antenna with three loops introduces three capacitance, i.e., the capacitance C_1 , C_2 and C_3 in Figure 6 (a). According to the transmission line theory [31] we derive and then plot the equivalent circuit in Figure 6 (b), where these three capacitors are connected in parallel. We therefore model the overall capacitance of the antenna as:

$$C_a = C_1 + C_2 + C_3 \quad (4)$$

We calculate the exact value of each capacitor using Equation 3. When worn by a human, our contact lens will be covered with tears. We model the tears as a dielectric layer which introduces three parasitic capacitors to the antenna, just as shown in Figure 6 (c). We still apply the Equation 3 to calculate the capacitance of these three capacitors, except using a different permittivity value ϵ_r , since we use polydimethylsiloxane (PMDS) as the substrate of the tag antenna whose permittivity is different from tears. In the end, we calculate the capacitance introduced by tears as:

$$C_t = C_1^t + C_2^t + C_3^t \quad (5)$$

The human eye consists of cornea, lens, vitreous humor and sclera, whose permittivities are different from each other. We use a similar method to model the capacitance introduced by each eye component and calculate the overall capacitance of the tag antenna as:

$$C = C_a + C_t + C_c + C_l + C_s + C_v \quad (6)$$

where C_c , C_l , C_s and C_v are the the capacitance introduced by the eye cornea, lens, sclera and vitreous humor, respectively.

Takeaway: The capacitance of the tag antenna is significantly affected by three structural parameters: the length of the conductive line, the line width of each loop and the gap between loops.

Resistance. The circular antenna with multiple loops consists of multiple circular conductive lines and turns that concatenate the circular lines together. When operating in low frequency, the current is evenly distributed within the conductor, just as shown in Figure 7,

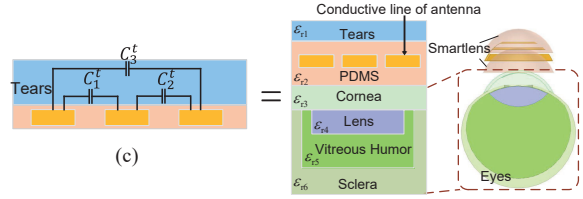


Figure 6: The capacitance introduced by the tag antenna and the tears.

so we can model the equivalent resistance of such a structure using the classical transmission line equivalent resistance model [43]:

$$R = \frac{1}{\sigma} \left(\frac{l}{wd} \right) \quad (7)$$

where σ is the *electrical conductivity* of the conductor material, d is the thickness of the conductive line (a constant of $10 \mu m$ in our structure), l and w are the total length and width of the conductive line, respectively, as shown in Figure 5.

The operating frequency also affects the resistance, so we need to extend Equation 7 to high frequencies. The higher the operating frequency, the more concentrated the electrical charge distributes within the conductive line's surface, just as shown in Figure 7. The uneven charge distribution enlarges the path by current travels and thus increases the resistance. We model the impact of such phenomena as:

$$R_{sk} = R \cdot \frac{d}{\delta \cdot (1 - e^{-d/\delta}) \cdot \frac{w+d}{w}} \quad (8)$$

where δ is a parameter that describes how deep an electromagnetic wave can penetrate a conductor, which is determined by the operating frequency f , the *magnetic permeability* μ and the electrical conductivity σ of the object [13]:

$$\delta = \sqrt{\frac{1}{\pi \sigma \mu}} \quad (9)$$

The conductor is copper, whose magnetic permeability and electrical conductivity are $1.256629 \cdot 10^{-6} H/m$ and $58.7 \cdot 10^6 Siemens/m$. Therefore, the δ value is $2.17 \mu m$ at operating frequency of $920 MHz$. *Takeaway:* The resistance of the antenna varies with the following two structural parameters: the length and width of the conductive lines.

Inductance. Based on the current sheet approximation [34] and transmission line model, we can get the specific inductor of our structure as follow:

$$L = \frac{\mu n^2 d_{avg}}{2} \left(\ln(2.46/\rho) + 0.2\rho^2 \right) \quad (10)$$

where n is the number of loops and μ is the magnetic permeability of the conductive line. The d_{avg} is the average diameter of all the loops:

$$d_{avg} = \frac{(d_{in} + d_{out})}{2} \quad (11)$$

where the d_{in} and d_{out} is the inner and outer radius of the whole antenna, as shown in Figure 5. The ρ is the fill ratio of the antenna which is represented by:

$$\rho = \frac{d_{out} - d_{in}}{d_{out} + d_{in}} \quad (12)$$

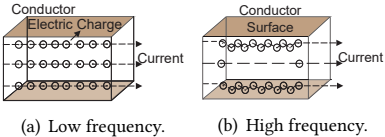


Figure 7: The distribution of electrical charge in the conductor.

Figure 8: Iterative refinement flow.

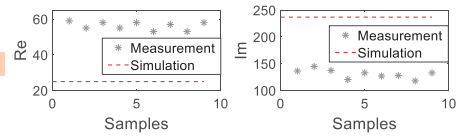


Figure 9: Comparison of simulation and measurement impedance test.

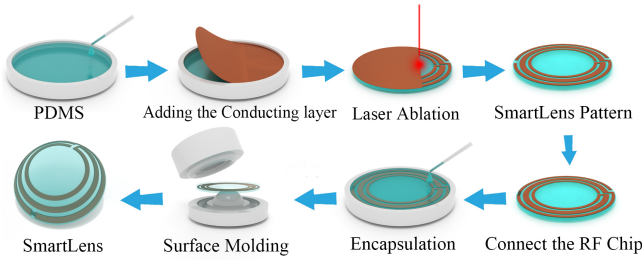


Figure 10: The workflow of the tag fabrication.

The w and s are the width and distance between two conductive lines as shown in Figure 5.

Takeaway: The inductance of the antenna varies with the following structural parameters: the number of loops, the width and gap between two conductive lines, and the diameter of the inner and outer radius of the antenna.

Impact of the material of the substrate and the conductive line. The permittivity ϵ_r of the substrate medium affects the capacitance of the antenna, just as shown in Equation 3. The material of the conductive line affects both the resistance and inductance of the antenna. Specifically, according to Equation 8, the electrical conductivity σ , the thickness d and the magnetic permeability μ of the conductive line affect the tag resistance. The magnetic permeability μ of the conductive line also affects the inductance as shown in Figure 5.

We note that the impact on the resistance and reactance of the antenna is known if the material is selected. SmartLens adopts PDMS [48] as the substrate medium, since PDMS is a non-toxic, non-hazardous material with good electrical insulation properties and is also one of the most commonly used materials for contact lenses. The permittivity ϵ_r of PDMS is 2.75. We choose copper as our conductive material due to its high electrical conductivity and ductility, whose electrical conductivity σ and magnetic permeability μ are $58.7 \cdot 10^6$ Siemens/m and $1.256629 \cdot 10^{-6}$ H/m, respectively. To avoid irritating the eyes with copper, we set the thickness d of the copper film to 10 μm and embed the copper in the PDMS.

Overall impedance of the antenna. According to the above analysis, we model the impedance of the antenna by combining Equation 2, Equation 8, Equation 10, and Equation 6. We also observe that the loop width, the gap between loops and the total length of the conductive line are three major structural parameters that affect the overall impedance of the antenna.

3.3.2 Solving the impedance matching equation. With the antenna impedance model, we are now able to solve the impedance matching equation:

$$Z_a = Z_{tag} \quad (13)$$

where Z_{tag} is the impedance of the RFID chip whose value is $30.53 - 211.81j$. We need to solve the equation to obtain the three structural parameters: the width of loop, the gap between loops and the length of the conductive line. The length determines the number of loops the antenna has. To simplify the problem, we fix both the width of each loop and the gap between loops. At the same time, to provide higher flexibility, we allow the antenna to change the width and gap across loops, just as shown in Figure 5. Therefore, we have more than three structural parameters, e.g., six parameters if we have three loops. We note that there may exist more than one solution to the non-linear Equation 13. We filter out certain solutions according to two criteria: first, the antenna created by the structural parameters should be within our space budget; second, according to the actual workmanship, the minimum gap between loops should be larger than 0.1 mm, i.e., the minimum scale that can be achieved by the laser engraving machine.

3.3.3 Iterative refinement. We derive the tag's base structure by solving the impedance matching equation in Section § 3.3.2. In practice, our tag antenna needs to be further curved to fit the human eyes. We note that, it is hard to evaluate the impact of the curving operation on the antenna's capacitive, inductive, and resistance. We therefore rely on simulation software to emulate the impact of 3D curving and finalize our design. Specifically, we input the derived antenna structural parameters and the 3D shape of the eyes into the simulation software, within which we curve our antenna to fit the human eyes. After 3D curing, the tag's impedance changes, so we adjust the structural parameters of the antenna inside the software to approach the impedance matching state. Without an analytical model, the parameter searching becomes a greedy search, which is computationally intensive, even though our derived structural parameters provide a very close-to-optimal starting point.

We adopt the particle swarm optimization (PSO) algorithms to guide our search. When we finish simulating using one set of structural parameters, we get the impedance of the antenna, which is fed into the optimization algorithms to calculate the fitness between tag impedance and the target we preset in advance. We adjust the structure parameters by tracking the changing speed and position of the parameters. Once we update a new combination of the structure parameters, we deliver it to the simulation software to get the simulation result of the current structure. When the fitness function converges, we get an optimal combination of structure parameters.

The last step is to fabricate the tag antenna according to the derived antenna structure and test its real impedance. We note that, due to engineering deviations in the actual manufacturing process, the impedance of the fabricated tag always diverges from the target value. For example, Figure 9 depicts the measured impedance together with our target impedance for one batch of fabricated antennas, from which, we observe that there exists a constant gap

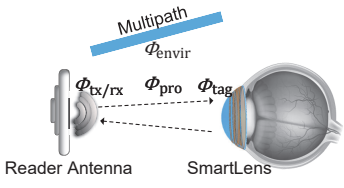


Figure 11: Phase components when eyelids are open and the eyeball is static.

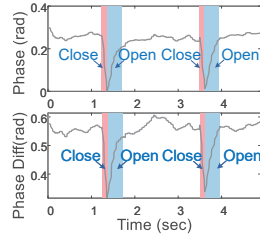


Figure 12: Phase variation caused by blink.

between the impedance obtained from antenna simulation and fabrication. To reduce the effect of engineering deviation effectively, we update the simulation objective based on the difference between the simulation and actual measurement as shown in Figure 8, and iterate until the tag antenna matches our target. We repeat the above process for multiple solutions of the impedance equations and pick the one with the best performance.

3.4 Tags Fabrication

Figure 10 depicts the fabrication process of SmartLens. We use the classic configuration ratio (base silicon: curing agent = 10 : 1) to get the prepolymer PDMS solution and then obtain PDMS films with thickness of 100 μm via spinning coating. We shape the copper film with its oxide layer stripped according to the desired tag antenna structure derived in Section § 3, and then laminate the shaped copper film to the uncured PDMS film (Sylagard 184, Dow Corning). Finally, the whole structure is encapsulated with PDMS and transferred to a contact lens mold for thermal curing (80° for 2 hours).

4 EYE MOVEMENT DETECTION

In this section, we introduce the algorithm we developed to detect eye movement from the backscattered signal.

4.1 Signal Model

We build the model of the backscattered signal in this section. We start from a simple but most common case, where the eyelid is open, the eyeball is static, and the eye is looking forward. We then extend our model to eye blinks and mobile cases where the eyeball rotates. We note that, in this section, we assume the human is static and only the eyeball and eyelid are allowed to move. We cover mobile scenarios in Section § 4.3.

Static eyeball with eyelid open. When the eyelids are open and the eyeball is static, the tag directly receives and backscatters the signal, just as shown in Figure 11. The phase shift between the transmitted and received signals is primarily determined by the distance between the tag and the receiver, as well as the hardware induced phase shift at the reader, which is given as:

$$\phi_{static} = \phi_{pro} + \phi_{tx/rx} + \phi_{tag} + \phi_{envir} \quad (14)$$

where ϕ_{pro} is the phase shift induced by signal propagation along the Line-of-Sight path, whose value is given by:

$$\phi_{pro} = \text{mod}\left(\frac{2\pi d}{\lambda}, 2\phi\right) \quad (15)$$

where λ is the signal wavelength, d is twice the distance from the tag to the reader. The phase offset $\phi_{tx/rx}$ is caused by the reader's transmission and receiving hardware circuitry. The phase offset ϕ_{tag} is induced by the backscattering of the tag's antenna. The phase shift ϕ_{envir} is caused by multipath interference in the environment as well as the individual's activity.

Eye blink. One eye blinking consists of one eyelid closing action and one eyelid opening action that happens within a very short period of time (typically 100 – 400 ms). When the eyelids are open, the phase of the backscattered signal is given in Equation 14. When the eyelids are closed, the signal needs to pass through the eyelids before reaching the tag. The eyelids introduce an additional phase shift ϕ_{eyelid} to the backscattered signal:

$$\begin{aligned} \phi_{close} &= \phi_{pro} + \phi_{tx/rx} + \phi_{tag} + \phi_{envir} + \phi_{eyelid} \\ &= \phi_{static} + \phi_{eyelid} \end{aligned} \quad (16)$$

By detecting the phase shift caused by the eyelids, we can then detect the blinking action.

Eye movement. Eye movement refers to transferring our gaze from one point to another by rotating the eye. The backscatter tag inside the contact lens moves with the eyeball rotation, which changes the phase of the backscattered signal. After carefully checking Equation 14, we observe that the phase offsets $\phi_{tx/rx}$, ϕ_{tag} , ϕ_{envir} are induced by the reader transmitter-receiver circuit, tag antenna impedance, and multipath interference respectively, and thus are constant. Only the phase offset ϕ_{pro} induced by the propagation via LoS path changes with the eye movements. Accordingly, we model the phase $\phi_{mobile}(t)$ of the received signal when the eyeball rotates as:

$$\phi_{mobile}(t) = \phi_{pro}(t) + \phi_{tx/rx} + \phi_{tag} + \phi_{envir} \quad (17)$$

The time-varying phase $\phi_{mobile}(t)$ can be used for detecting the direction of the eyeball rotation.

4.2 Sensing the Eye Activities

In this section, we describe the algorithm that senses eye activities, including blink and eyeball rotation, using the phase of the received backscattered signal.

4.2.1 Sensing the blink. We detect eye blinking by identifying the phase change caused by closing and reopening the eyelids. An example is given in Figure 12, from which we see an obvious phase change when the human closes his/her eyelid. The human will reopen the eyelid soon and the phase recovers. We also observe that the speed of eyelid closing is much faster than reopening.

4.2.2 Sensing the eye movement. We leverage the phase variations to sense the movement of the eyeball, including moving in one direction and rotation. We use the example in Figure 13 to better illustrate the sensing algorithm, where we deploy a reader on the left side of the human, on the azimuth plane. We take the direction of looking straight ahead as the reference position, since it is the most common and comfortable position of the eyeball.

Moving in single direction. The signal phase varies with the relative distance between the tag and the reader antenna. For the reader antenna on the azimuth plane, the distance d decreases when the eyes move to the *left*, resulting in decreasing phase $\phi_{mobile}(t)$ according to Equation 15 and 17. From our empirical results, we

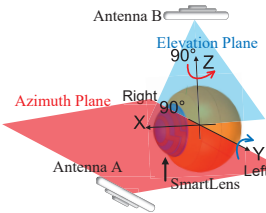


Figure 13: The locations of the eyeball, the SmartLens tag, and the readers in 3D space.

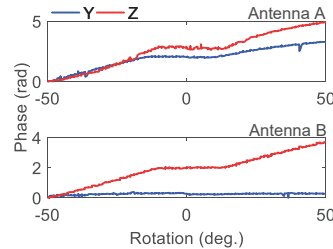


Figure 14: The rotation of SmartLens tag along Y and Z axis introduces phase variations.

observe that, except the tag-reader distance, the polarization also affects the phase of the received signal. SmartLens's tag antenna is a linear-polarized dipole, whose polarization direction is along the Y-axis in the example depicted in Figure 13. On the other hand, the reader's antenna is a circular-polarized antenna that consists of two perpendicular dipoles. When the SmartLens tag rotates, there exist mismatches in polarization direction between the reader and tag antenna, causing phase variations.

To demonstrate the phase variations caused by polarization direction mismatch, we measure the phase of the received signal by fixing the tag-reader distance and only rotating the tag along Y and Z axis. We plot the results in Figure 14 *upper*, from which we observe that when the tag rotates to *left* and *right*, the phase of the signal received by the antenna in the azimuth plane respectively decreases and increases, which matches with the phase variation pattern caused by tag-reader distance changes. We also observe that, the phase variations caused by tag rotation along the Y-axis are similar to the phase variations caused by rotation along the Z-axis. Therefore, purely relying on the phase variations of the signal received by the antenna in the azimuth plane cannot differentiate *left* from *down* and *right* from *up*.

To solve this problem, we deploy another antenna on the elevation plane, as shown in Figure 13. The up and down for the antenna in the azimuth plane becomes left and right in the elevation plane, so the relationship between the distance and the phase of the received signal still remains. To investigate the impact of polarization direction on the phase of received signal, we repeat the above experiments using the antenna on elevation plane and plot the results in Figure 14 *lower*, from which we see that the rotation along Z-axis causes similar phase variations as those with the antenna on azimuth plane, but the rotation along Y-axis introduces negligible phase changes on the received signal. By combining the phase variations of two antennas, we are able to remove the ambiguity and identify four directions of eyeball rotation. For example, when the eyes move *down*, the signal phase decreases for the antenna in azimuth plane, but increases for the antenna in elevation plane, as shown in Figure 15.

Looking in a single direction and rotation. On top of the detected eyeball movement in a single direction, we further define two types of operations that consist of multiple eyeball movements: *looking in one direction* and *rotation*. Looking in one direction consists of two segments of eye movements with opposite directions, for example, looking left consists of moving eyes to the left and then moving right to its initial position. On the other hand, rotation

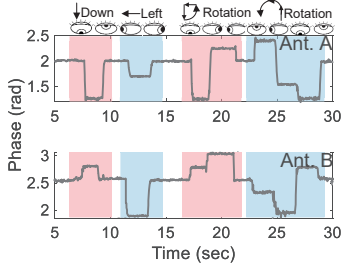


Figure 15: Recognizing eye movement by combining phase measured from two antennas.

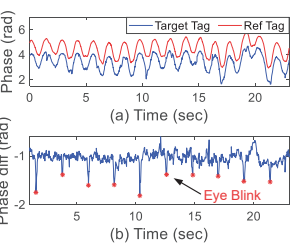


Figure 16: Raw phase data VS phase differences.

consists of two segments of eye movements with non-opposite directions, for example, moving eyes to the left and then up. Just as shown in Figure 15, by grouping two consecutive eye movement together, we are able to recognize the operation of looking in single direction and rotation.

4.3 Interference from Human Activities

Eye movements are highly likely accompanied by other human activities such as turning the head, walking, or running. Those activities may cause phase variations in both ϕ_{pro} and ϕ_{envir} . To demonstrate the impact of human motion, we fix a bionic eye to a volunteer's head and let the volunteer walk at a speed of 3 km/h. We measure the phase of the backscattered signal when the bionic eye performs eye blinks repeatedly and plot the results in Figure 16 (a), from which we could see that no blinks can be observed.

To address the issue, we employ the phase differential to determine the changes in eye movement. To mitigate the interference of irrelevant human activities, we propose attaching a third reference backscatter tag to the head. Since the reference tag and two SmartLens tags are close and static to each other, they experience similar ϕ_{envir} , even when the head moves. Therefore, the phase difference between the reference tag and two SmartLens tags is close to constant if there are no eye activities, just shown in Figure 16 (b). The phase difference varies when and only when there exists eye movement, such as the eye blink or rotation. We therefore use the phase difference between reference tag and SmartLens tag as the signal and apply the aforementioned techniques to sense the eye activities.

5 EVALUATION

We evaluate the performance of SmartLens in this section. We first present the end-to-end performance, followed by the investigation of the impact of various system parameters on the performance. In the end, we verify SmartLens's performance under biological impact.

5.1 End-to-end Performance

Methodology. We use an Impinj Speedway R420 RFID reader [19] with two 10 dBi panel directional antennas [42] as the transceivers. To emulate the eye movement, we conduct our experiments using a bionic eye, which is fixed on volunteers' head, just as shown in Figure 21. We wear SmartLens tag on the bionic eye and attach the reference tag at 7 cm away. By default, the transmission power of the reader is 32 dBm. We set the trajectory of the bionic eye and

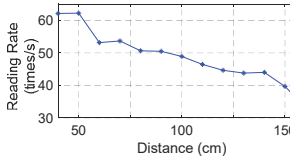


Figure 17: Reading rate of SmartLens at different tag-reader distances.

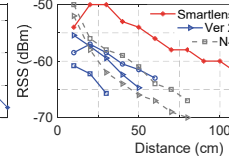


Figure 18: The RSS of signal received by different versions of SmartLens tag and two commercial RFID tags.

the movement angle in advance to obtain the ground truth of the eye movement.

Communication range and tag efficiency. We investigate the SmartLens tag's maximum communication range by measuring the tag's reading rate achieved with varying distances between the reader antenna and the bionic eye. Figure 17 depicts the reading rate, from which we see that the SmartLens tag can communicate reliably up to 1.5 m from the receiving antenna. Although the tag's maximum communication distance is 1.6 m, the tag's average reading rate drops significantly beyond 1.5 m, making it unsuitable for eye-tracking detection. To provide more context of SmartLens tag's communication range, we also compare it with two commercial RFID tags, N40 (40×21 mm) and B42 (22×8 mm), both of which have comparable size with SmartLens tag. Under the same conditions, we plot the RSS of these tags at different distances. We plot the RSS of the signal backscattered by these tags at varying distance in Figure 18. The results demonstrate that the communication range of SmartLens is 1.87 times greater than that of commercial tags of comparable size. In addition, we plot the RSS of several versions of the SmartLens tag generated during the parameter optimization in the figure, which verifies the necessity of optimizing the structure of tag antenna.

Accuracy in static environments. We investigate the detection accuracy for nine types of eye movement: the eye blink, four types of looking in one direction and four types of rotation. We fix the bionic eye on the table in an $7.6\text{ m} \times 7.6\text{ m}$ office, just as shown in Figure 21 (a) and configure the bionic eye to repeat the above nine types of eye movement for 100 times at varying distances from the reader. We plot the confusion matrix in Figure 19, from which we see that the eye blink and eye movement detection accuracy are above 89% and 92% respectively. We also plot the average true positive rate and false negative rate of detecting nine types of movements achieved with varying tag-reader distance in Figure 20. We see that the true positive rate still maintains at higher than 0.79 even when the tag-reader distance is 1.5 m.

Accuracy in mobile scenarios. To evaluate SmartLens's performance in mobile scenarios, we conduct experiments on volunteers with three types of movement:

(a). *Subtle movement.* We deploy SmartLens in the office and place one antenna on the ceiling and another antenna beside the human body, as illustrated in Figure 21 (b). A volunteer is asked to fix the bionic eye on his head and work normally. We pre-program the bionic eye to mimic nine types of eye movements, each for 100 times at one tag-reader distance. We use the reader to continuously capture eye movements for 40 minutes at different distances. We

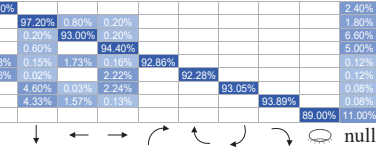


Figure 19: The confusion matrix of recognizing nine types of eye movement.

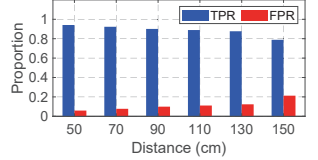


Figure 20: The TPR and FPR of recognizing nine types of eye movement achieved at varying tag-reader distances.

plot the detection accuracy in Figure 22 (a), from which we observe that the average detection accuracy of all nine types of eye movements are 96.11%, 92.29%, 90.07%, 88.93%, 87.67% and 78.87% when the tag-reader distance changes from 50 cm to 150 cm.

(b). *Moderate movement.* We repeat the above experiments by letting the volunteer perform two types of activities that involve moderate body movement: walking on a treadmill at a speed of 3 km/h and playing a racing game, just as shown in Figure 21 (c). We plot the detection accuracies achieved at varying tag-reader distances in Figure 22 (b). The average detection accuracy of all nine types of eye movements are 95.96%, 93.79%, 91.71%, 86.99%, 83.40% and 74.47% when the tag-reader distance changes from 50 cm to 150 cm.

(c). *Highly dynamic movement.* We repeat the experiments by letting one volunteer jog at 5 km/h , as shown in Figure 21 (d). Similarly, we test the bionic eye's eye-movement recognition accuracy at different tag-reader distances and plot the results in Figure 22 (c). The average detection accuracies of all nine types of eye movements are 95.79%, 90.77%, 87.70%, 83.71%, 80.51% and 73.73% when the tag-reader distance changes from 50 cm to 150 cm, demonstrating SmartLens's robustness under highly dynamic movements.

Detection angle. We fix the tag-reader distance at 80 cm and place the bionic eye on a rotator, which is utilized to accurately control the rotation angle of SmartLens tag. We measure the phase of the backscattered signal when the tag rotates to different angles and plot the results in Figure 23. We observe from Figure 23 (a) that, when the tag is at certain angles, the antenna beside the human body (Antenna A) enters a blind zone where no backscattered signal can be received. The location of the blind zone is determined by the tag's radiation pattern. We see from Figure 23 (b) that the signal reflected by the tag is weak in the direction that is perpendicular to the tag (or the Z-X plane in this example). Therefore, when the weak direction is pointing at the reader's antenna, the reader enters the blind zone. We note that the possible angles of the human eyes could rotate to within the range of $\pm 50^\circ$, which are fully covered by SmartLens's tag.

5.2 Performance with Different Parameters

Impact of reference tag's position. We examine the impact of the reference tag's position. As shown in Figure 24 (a), we attach the reference tags to different positions around the ears and eyes. We program the eye movements of the bionic eyes and invite a volunteer to sit in front of the table. We place the reader's antenna at 90 cm apart from the eyes. Figure 24 (b) depicts the accuracy of identifying distinct eye movements, from which we see that SmartLens achieves more than 93.13% recognition accuracy at all

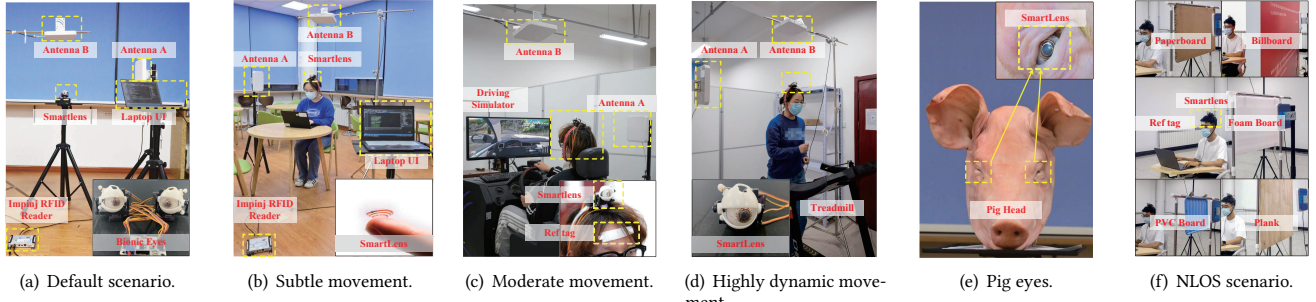


Figure 21: Different scenarios. (a) Stationary scenario with no interference. (b) Office scenario with the multipath. (c) Simulated driving scenario with dynamic multipath. (d) Dynamic human motion with the most interference. (e) Biological tissue environment. (f) Different NLOS environments.

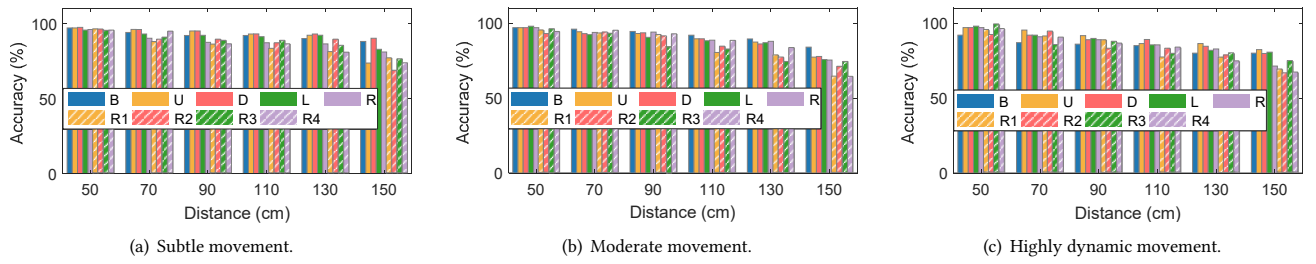


Figure 22: Accuracy of eye movement detection in different scenarios. (The actions of eye blink, looking up, down, left, and right, and rotating from up to right, right to down, down to the left, and left to up are represented with b , u , d , l , r , R_1 , R_2 , R_3 , R_4 respectively)

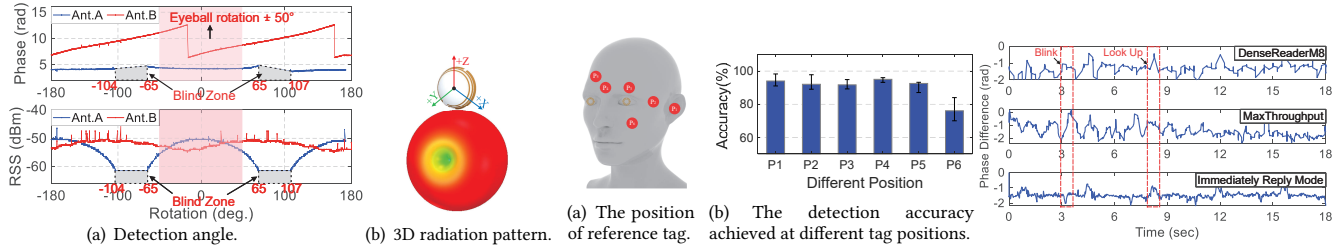


Figure 23: The detection angle and 3D radiation pattern of SmartLens.

positions near the eyes or ears. The tag location at the cheek is less preferred since the recognition accuracy drops to 75.9%. The reason of the performance drop is that the cheek muscles move when the human talks or eats, resulting in changes in the relative position between the reference tag and the SmartLens tag.

Impact of tag reading rate. Ensuring high tag reading rate is critical for tracking eye movement accurately. Since the eye rotation drives tag movement at a rate ranging from 30 deg/s to 500 deg/s , inadequate tag reading rate may miss the continuous phase changes caused by the rapid eye movement, causing ambiguity in detecting the tag's displacement. To avoid phase ambiguity, we must read the tag at a minimum rate of 4 Hz to 76 Hz .

Impinj's Speedway reader [38] has a number of predefined reading modes. We set the reader in two modes: the *DenseReaderM8* mode, which has the most interference tolerant capability and *Maxthroughput* mode, which can provide the fastest data rate, and compare the eye movement detection accuracy in the default deployment environment. As illustrated in Figure 25, when the

Figure 24: The detection accuracy varies with reference tag's position.

amount of interference other than eye movement gradually increases, the *DenseReaderM8* is limited by the reading rate (22.8 Hz) and thus cannot accurately detect the eye movement. While the *Maxthroughput* (47 Hz) mode improves the reading rate in comparison to *DenseReaderM8*, it is still unable to capture eye movements in the dynamic environment. As a result, we resolve this issue using the method described in [52], which achieves a sampling rate of 100 Hz by configuring the reader to immediately report reading whenever the tag is detected.

Impact of eye movement speed. To determine the impact of eye movement speed on the recognition accuracy of the SmartLens, we set the eye movement speed of the bionic eye to 30 degs/s , 100 degs/s , and 500 degs/s , and then test the accuracy of eye movement recognition at various distances under the default scenario shown in Figure 21 (a). We plot the measured detection accuracy in Figure 26, from which we see that the average identification accuracy for eyeball rotation under different speeds is 89.81%, 91.35% and 79.92%, respectively. At the same sampling

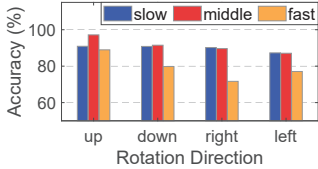


Figure 26: The detection accuracy under different speeds of eye movement.

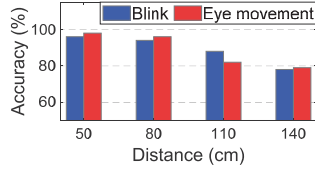


Figure 27: The detection accuracy of eye movements under environmental interference.

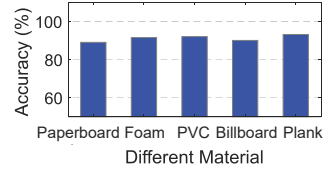


Figure 28: The detection accuracy of eye movements in different NLoS.

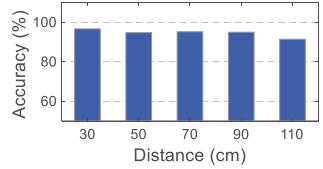


Figure 29: The detection accuracy of eye movements with SmartLens wear on the pig eyes.

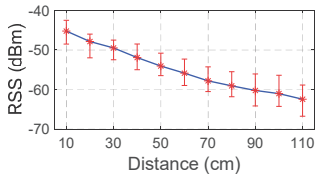


Figure 30: The measured RSS at varying tag-reader distances, when the SmartLens tag is worn on the pig eyes.

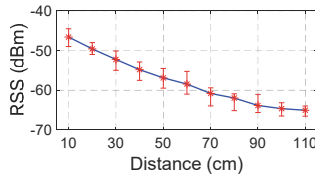


Figure 31: The measured RSS at varying tag-reader distances, when the SmartLens tag is worn on the pig eyes with tear films.

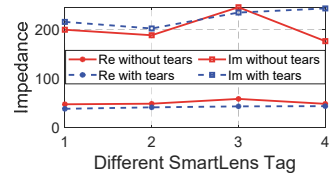


Figure 32: The measured antenna impedance when the SmartLens tag is worn on pig eyes with or without tears.

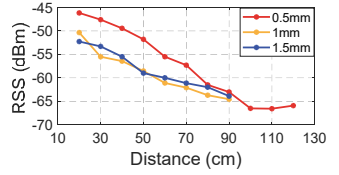


Figure 33: The measured RSS at varying tag-reader distances, when the SmartLens tag is worn on the pig eyes with varying eyelid thicknesses.

rate, as the eye rotation speed increases, the system’s capacity to detect fast eye movements reduces.

The impact of environmental interference. To validate SmartLens’s robustness under environmental disturbances, we fix the bionic eyes on the head of one static volunteer and ask another volunteer to randomly move around. We continuously estimate the movement of the bionic eyes and compare the estimates with the ground truths. We repeat the experiments by varying the distance between the reader’s antenna and the bionic eyes. The accuracy of eye movement recognition at various distances is depicted in Figure 27. We see from the figure that the average recognition accuracy of SmartLens decreases when interference exists, but the overall recognition accuracy remains above 78%, demonstrating SmartLens’s robustness in the presence of interference.

Performance in non-line-of-sight (NLoS) scenarios. We create NLoS scenarios by placing different blocking objects between the SmartLens tag and the reader antenna, just as shown in Figure 21 (f), including a foam board ($70\text{ cm} \times 50\text{ cm} \times 5\text{ cm}$), a PVC board ($50\text{ cm} \times 38\text{ cm} \times 0.2\text{ cm}$), a paperboard ($80\text{ cm} \times 55\text{ cm} \times 2\text{ cm}$), a plank ($80\text{ cm} \times 80\text{ cm} \times 1.5\text{ cm}$), and a billboard ($320\text{ cm} \times 240\text{ cm} \times 12\text{ cm}$). The billboard consists of two printed cloths supported by a metal frame. The printed cloth is made of vinyl and polyester yarn. In each NLoS setting, we program the bionic eyes to perform all the eye movements, each repeated 100 times. Figure 28 shows the detection accuracy under different NLoS settings, from which we see that the average detection accuracy remains at 91.1%.

5.3 Biological Impact on the Performance

Pig eyes are widely used in biological research [35, 45] to imitate human eyes, since they share similar anatomical and physiological properties. Approved by the IRB of our university, to investigate the biological impact of tissues on SmartLens’s performance, we evaluate SmartLens in three distinct ocular settings, including pig eyes with tears, eyelids, and different eyeball shapes.

The biological impact of pig eyes. To test SmartLens’s performance on pig eyes, we wear the SmartLens tag on the pig’s eyes, as shown in Figure 21 (e), and manually rotate the pig’s eyes by 20 degrees on four directions (up, down, left and right). We vary the tag-reader distance from 30 cm to 110 cm and repeat each rotation 100 times at each distance. We plot the eye movement detection accuracy in Figure 29, from which we see that the accuracy is still high, i.e., 94.61%, even when the tag-reader distance reaches 1.1 m .

The impact of eyeball shapes. The pig eyes have similar size ($21.6 - 23.9\text{ mm}$ [10]) with the human eyes ($22.0 - 24.8\text{ mm}$ [6]), which makes them a good experimental material for evaluating the impact of eyeball shape. We, therefore, wear the SmartLens tag on the 10 different pig eyes and measure the signal strength of the backscattered signal. We repeat the experiments by varying the tag-reader distance and plot the measured results in Figure 30. We see from the figure that different pig eyes cause an average of 6.56 dBm RSS difference across tag-reader distances. We also observe that the measured RSS decreases with tag-reader distance, but the maximum communication ranges are similar for these 10 pig eyes. The result indicates that the performance of SmartLens on eyes of different shapes is stable.

The impact of tears. The area surrounding the human eye is filled with tears, which are primarily composed of water and protein. In order to investigate the impact of tears, we test the communication efficiency of SmartLens on different pig eyes using artificial tears. We measure the strength of the signal backscattered by the tag and plot the results in Figure 31. The variance in RSS at various distances is approximately 4.26 dBm on average. The communication range of SmartLens tag is 80 cm on one pig eye #1, 90 cm on another pig eye #2, 100 cm on pig eye #3 – #6, and 110 cm on the rest of pig eyes #7 – #10. The reason of the communication range decreasing is that tears change the substrate of the SmartLens tag, which affects the impedance of the tag antenna. We use a network vector analyzer to

measure the impedance of the SmartLens antenna with and without tears and plot the results in Figure 32. We clearly see the impedance of tags with tears is different from the tag without tears, and the introduced impedance variations are different across tags. The results show that tears indeed affect communication performance of SmartLens. However, SmartLens still maintains a minimum of 1 *m* communication range when worn on all 10 pig eyes.

The impact of the thickness of the eyelid. To investigate the impact of eyelid thicknesses on the communication performance of SmartLens, we wear the SmartLens on selected pig eyes, whose eyelid thickness is similar to that of human (approximately 0.7 *mm* – 1.5 *mm* according to [18]). We measure the strength of the backscattered signal at different tag-reader distances and plot the result in Figure 33. We see that the eyelid thickness indeed affects the communication range of the SmartLens tag: the thicker the eyelid, the shorter the communication range. We note that, SmartLens can still maintain a communication range of 90 *cm* using commercial RFID reader when the eyelid thickness is 1.5 *mm*.

5.4 Case study: Controlling the Cursor

SmartLens provides a low-cost and low-power eye tracking solution and thus enables various human computer interaction applications. More importantly, SmartLens works in the dark and requires no LOS between the tag and the reader, making itself a complementary to existing vision-based eye tracking solutions. In this section, we prototype a SmartLens based cursor controlling demo system. Our demo system uses the *tkinter* module on the Python 3.7 platform, and implements the following three modules.

Data pre-processing module. The data received by the reader is transmitted to the backend server. The backend server intercepts the tag EPC, phase, and timestamp and divides the received data into four groups: signal from target tag and ref tag received by Antenna 1, and signal from target tag and ref tag information received by Antenna 2. We then apply time-domain interpolation and Kalman filtering to the signal in each group. The interpolation interval is set to 10 milliseconds. At last, we unwrap the phase and the pre-processed data is input to the following modules.

Eye movement identification module. This module takes the data generated by the data pre-processing module as input and implements the algorithms we described in Section § 4.2 to identify the type of eye movement.

Cursor controlling and trajectory displaying module. In this prototype, we control the cursor by performing only one operation, i.e., looking in one direction. We identify the starting and ending timestamps of the operation and calculate its total moving time. We multiply a predefined constant speed (60 *pixel/s* in our current implementation) with the moving time to obtain the moving distance. Given the initial position of the cursor on the screen, the detected looking direction (up, down, left or right) and the calculated moving distance, we are able to plot the moving trajectory of the cursor on the screen, just as shown in Figure 34. We use blink as the command to clear the screen and move the cursor back to the center of the screen. We provide a demo video of SmartLens, which is available at: https://youtu.be/vAx_6-Ik2yk.

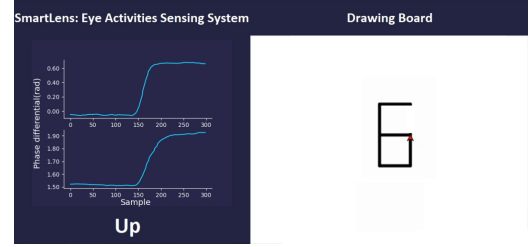


Figure 34: The user interface of our SmartLens based cursor controlling system: the received signal is displayed in real-time on the left hand side and the trajectory of the cursor is displayed on the right hand side.

6 LIMITATIONS AND FUTURE WORK

Detection range and reliability. Our results show that SmartLens works reliably when the tag-reader distance is within 1.5 *m*. When the tag-reader distance increases or the degree of human activity becomes stronger, the detection accuracy drops below 73%. There are multiple potential approaches to mitigate the problem, for example, designing smarter detection algorithms or using machine learning to separate eye movements in the presence of interference. We plan to explore these mechanisms in our future work.

Tag antenna design. SmartLens utilizes copper film as the conductive layer. In the next stage, we will investigate how to make the conductive layer fully transparent using novel materials such as multilayer graphene and PEDOT. We intend to use multilayer graphene as the conductive layer to replace the copper film. While multilayer graphene can achieve a communication distance up to 80 *cm* in the planar condition, when moved to a curved surface, the increased curvature causes internal graphene fracture, reducing the overall tag's conductivity. In the future, we will continue to investigate the curved conductive layer lamination process and conduct experiment with other transparent materials.

7 CONCLUSION

In this work, we present the design, implementation and evaluation of SmartLens, a wearable contact lens that can detect eye movement with zero power. Through both theoretical analysis and experiment evaluation, we demonstrate the effectiveness of the proposed system in tracking eye activities in real-world settings. We believe this is the first step towards the ambitious goal of meta eyes.

ACKNOWLEDGMENTS

This work is supported by the NSFC A3 Foresight Program Grant 62061146001, and the National Natural Science Foundation of China (61972316). This work is also supported by the International Cooperation Project of Shaanxi Province (2020KWZ-013). We thank our reviewers and shepherd for their insightful feedback which helped improve this paper. We would also like to thank Dr. Yuhui Ren for his help in early developments of the system. Xiaojiang Chen is the corresponding author.

REFERENCES

- [1] 2014. Introducing our smart contact lens project. <https://blog.google/alphabet/introducing-our-smart-contact-lens/>.
- [2] 2022. Inwith at CES 2022. <https://inwithcorp.com/envisioning-reality/>.
- [3] 2022. Mojo. <https://www.mojo.vision/mojo-lens>.
- [4] 2022. SmartLens. <https://github.com/Nisl-lly/Smartlens>.
- [5] Sharifa Alghowinem, Roland Goecke, Michael Wagner, Gordon Parker, and Michael Breakspear. 2013. Eye movement analysis for depression detection. In *2013 IEEE International Conference on Image Processing*. IEEE, IEEE, Melbourne, 4220–4224.
- [6] Inessa Bekerman, Paul Gottlieb, and Michael Vaiman. 2014. Variations in eyeball diameters of the healthy adults. *Journal of ophthalmology* 2014 (2014), 5.
- [7] Mehmet Cem Catalbas, Tomaz Cegovnik, Jaka Sodnik, and Arif Gulten. 2017. Driver fatigue detection based on saccadic eye movements. In *2017 10th International Conference on Electrical and Electronics Engineering (ELECO)*. IEEE, IEEE, Bursa, 913–917.
- [8] Xiangmao Chang, Jiahua Dai, Zhiyong Zhang, Kun Zhu, and Guoliang Xing. 2021. RF-RVM: Continuous respiratory volume monitoring with COTS RFID tags. *IEEE Internet of Things Journal* 8, 16 (2021), 12892–12901.
- [9] Jin-Chern Chiou, Shun-Hsi Hsu, Yu-Chieh Huang, Guan-Ting Yeh, Wei-Ting Liou, and Cheng-Kai Kuei. 2017. A wirelessly powered smart contact lens with reconfigurable wide range and tunable sensitivity sensor readout circuitry. *Sensors* 17, 1 (2017), 108.
- [10] Kwang-Eon Choi, Vu Thi Que Anh, Jong-Hyun Oh, Cheolmin Yun, and Seong-Woo Kim. 2021. Normative Data of Axial Length, Retinal Thickness Measurements, Visual Evoked Potentials, and Full-Field Electroretinography in Female, Wild-Type Minipigs. *Translational vision science & technology* 10, 12 (2021), 3–3.
- [11] Viviane Clay, Peter König, and Sabine Koenig. 2019. Eye tracking in virtual reality. *Journal of eye movement research* 12, 1 (2019).
- [12] SARAH DEWEERTD. 2020. Eyeing the connection between autism and vision. <https://www.spectrumnews.org/features/deep-dive/eyeing-the-connection-between-autism-and-vision/16-SEPTEMBER-2020>.
- [13] Daniel Dobkin. 2012. *The rf in RFID: uhf RFID in practice*. Newnes, newnes.
- [14] Gerardo Fernández, Pablo Mandolesi, Nora P Rotstein, Oscar Colombo, Osvaldo Agamenonni, and Luis E Politi. 2013. Eye movement alterations during reading in patients with early Alzheimer disease. *Investigative ophthalmology & visual science* 54, 13 (2013), 8345–8352.
- [15] Markus Frey, Matthias Nau, and Christian F Doeller. 2021. Magnetic resonance-based eye tracking using deep neural networks. *Nature neuroscience* 24, 12 (2021), 1772–1779.
- [16] Moshe Fried, Eteri Tsitsishvili, Yoram S Bonneh, Anna Sterkin, Tamara Wygnanski-Jaffe, Tamir Epstein, and Uri Polat. 2014. ADHD subjects fail to suppress eye blinks and microsaccades while anticipating visual stimuli but recover with medication. *Vision research* 101 (2014), 62–72.
- [17] S Zohreh Homayounfar, Sohe Rostamini, Ali Kiaghadi, Xingda Chen, Emerson T Alexander, Deepak Ganesh, and Trisha L Andrew. 2020. Multimodal smart eyewear for longitudinal eye movement tracking. *Matter* 3, 4 (2020), 1275–1293.
- [18] Kun Hwang. 2013. Surgical anatomy of the upper eyelid relating to upper blepharoplasty or blepharoptosis surgery. *Anatomy & Cell Biology* 46, 2 (2013), 93–100.
- [19] impinj. © 2012 - 2022 Impinj, Inc.. ImpinJ Speedway R420 RFID reader. <https://www.impinj.com/products/readers/impinj-speedway>.
- [20] Robert JK Jacob. 1993. Eye movement-based human-computer interaction techniques: Toward non-command interfaces. *Advances in human-computer interaction* 4 (1993), 151–190.
- [21] Cheonhoo Jeon, Jahyun Koo, Kyongsu Lee, Minseob Lee, Su-Kyoung Kim, Sangbae Shin, Sei Kwang Hahn, and Jae-Yoon Sim. 2019. A smart contact lens controller IC supporting dual-mode telemetry with wireless-powered backscattering LSK and EM-radiated RF transmission using a single-loop antenna. *IEEE Journal of Solid-State Circuits* 55, 4 (2019), 856–867.
- [22] Do Hee Keum, Su-Kyoung Kim, Jahyun Koo, Geon-Hui Lee, Cheonhoo Jeon, Jee Won Mok, Beom Ho Mun, Keon Jae Lee, Ehsan Kamrani, Choun-Ki Joo, et al. 2020. Wireless smart contact lens for diabetic diagnosis and therapy. *Science advances* 6, 17 (2020), eaba3252.
- [23] Marcin Kolodziej, Paweł Tarnowski, Dariusz J Sawicki, Andrzej Majkowski, Ramięgusz J Rak, Aleksandra Bala, and Agnieszka Pluta. 2020. Fatigue detection caused by office work with the use of EOG signal. *IEEE Sensors Journal* 20, 24 (2020), 15213–15223.
- [24] Mengtang Li, Quanlong Qiu, Jie Zhu, and Chao Gou. 2022. An Eye Tracking based Aircraft Helmet Mounted Display Aiming System. *IEEE TRANSACTIONS ON HUMAN-MACHINE SYSTEMS* 5, 3 (2022).
- [25] Tianxing Li and Xia Zhou. 2018. Battery-free eye tracker on glasses. In *Proceedings of the 24th Annual International Conference on Mobile Computing and Networking*. ACM, New Delhi, 67–82.
- [26] Zhaowei Li, Peiyuan Guo, and Chen Song. 2021. A review of main eye movement tracking methods. In *Journal of Physics: Conference Series*, Vol. 1802. IOP Publishing, IOP Publishing, IOP science, 042066.
- [27] Andrew R Lingley, Muhammad Ali, Y Liao, Ramin Mirjalili, Maria Klonner, M Sopanen, Sami Suikonen, Tueng Shen, Brian P Otis, H Lipsanen, et al. 2011. A single-pixel wireless contact lens display. *Journal of Micromechanics and Microengineering* 21, 12 (2011), 125014.
- [28] Jialin Liu, Dong Li, Lei Wang, and Jie Xiong. 2021. BlinkListener: "Listen" to Your Eye Blink Using Your Smartphone. *Proceedings of the ACM on Interactive, Mobile, Wearable and Ubiquitous Technologies* 5, 2 (2021), 1–27.
- [29] Yunju Nam, Upyong Hong, Hyeyoung Chung, and Soo Rim Noh. 2022. Eye Movement Patterns Reflecting Cybersickness: Evidence from Different Experience Modes of a Virtual Reality Game. *Cyberpsychology, Behavior, and Social Networking* 25, 2 (2022), 135–139.
- [30] Jihun Park, Joohee Kim, So-Yun Kim, Woon Hyung Cheong, Jiuk Jang, Young-Geun Park, Kyungmin Na, Yun-Tae Kim, Jun Hyuk Heo, Chang Young Lee, et al. 2018. Soft, smart contact lenses with integrations of wireless circuits, glucose sensors, and displays. *Science advances* 4, 1 (2018), eaap9841.
- [31] Clayton R Paul. 2007. *Analysis of multiconductor transmission lines*. John Wiley & Sons, John Wiley & Sons.
- [32] Elmar H Pinkhardt and Jan Kassubek. 2011. Ocular motor abnormalities in Parkinsonian syndromes. *Parkinsonism & Related Disorders* 17, 4 (2011), 223–230.
- [33] Md Moklesur Rahman, Toufiq Aziz, and Heung-Gyo Ryu. 2021. UHF RFID Wireless Communication System for Real Time ECG Monitoring. In *2021 Twelfth International Conference on Ubiquitous and Future Networks (ICUFN)*. IEEE, IEEE, Jeju Island, 276–279.
- [34] Edward Bennett Rosa. 1906. *Calculation of the self-inductance of single-layer coils*. US Government Printing Office, Washington.
- [35] Irene Sanchez, Raul Martin, Fernando Ussa, and Ivan Fernandez-Bueno. 2011. The parameters of the porcine eyeball. *Graefe's Archive for Clinical and Experimental Ophthalmology* 249, 4 (2011), 475–482.
- [36] Lauren M Schmitt, Edwin H Cook, John A Sweeney, and Matthew W Mosconi. 2014. Saccadic eye movement abnormalities in autism spectrum disorder indicate dysfunctions in cerebellum and brainstem. *Molecular autism* 5, 1 (2014), 1–13.
- [37] Monica Siqueiros Sanchez, Terje Falck-Ytter, Daniel P Kennedy, Sven Bölte, Paul Lichtenstein, Brian M D'Onofrio, and Erik Pettersson. 2020. Volitional eye movement control and ADHD traits: a twin study. *Journal of Child Psychology and Psychiatry* 61, 12 (2020), 1309–1316.
- [38] James Skinner. 2021.11.9. Reader Modes (RF Modes) Made Easy. <https://support.impinj.com/hc/en-us/articles/360000046899-Reader-Modes-RF-Modes-Made-Easy>.
- [39] Federico M Sukno, Sri-Kaushik Pavani, Constantine Butakoff, and Alejandro F Frangi. 2009. Automatic assessment of eye blinking patterns through statistical shape models. In *International Conference on Computer Vision Systems*. Springer, Springer, Belgium, 33–42.
- [40] Joseph J Tecce, James Gips, C Peter Olivieri, Linen J Pok, and Michael R Consiglio. 1998. Eye movement control of computer functions. *International Journal of Psychophysiology* 29, 3 (1998), 319–325.
- [41] Elisabet Tiselius and Kayle Snead. 2020. Gaze and eye movement in dialogue interpreting: An eye-tracking study. *Bilingualism: Language and Cognition* 23, 4 (2020), 780–787.
- [42] uniden cellular. uniden. Uniden® Indoor Panel Directional Antenna. <https://unidenellular.com/uniden-indoor-panel-directional-antenna-374.html>.
- [43] Brian C Wadell. 1991. *Transmission line design handbook*. Artech House Microwave Library, Norwood.
- [44] H Kenneth Walker, W Dallas Hall, and J Willis Hurst. 1990. Clinical methods: the history, physical, and laboratory examinations. *Butterworth Publishers* 8, 3 (1990).
- [45] E. M. Walters, M. S. Samuel, K. D. Wells, L. K. Riley, and R. S. Prather. 2011. THE PIG AS A BIOMEDICAL MODEL: HOW THE NATIONAL SWINE RESOURCE AND RESEARCH CENTER CAN HELP YOU. *Reproduction Fertility Development* 24 (2011).
- [46] Chuuy Wang, Lei Xie, Wei Wang, Yingying Chen, Yanling Bu, and Sanglu Lu. 2018. Rf-ecg: Heart rate variability assessment based on cots rfid tag array. *Proceedings of the ACM on Interactive, Mobile, Wearable and Ubiquitous Technologies* 2, 2 (2018), 1–26.
- [47] Haofei Wang, Jimin Pi, Tong Qin, Shaojie Shen, and Bertram E Shi. 2018. SLAM-based localization of 3D gaze using a mobile eye tracker. In *Proceedings of the 2018 ACM Symposium on Eye Tracking Research & Applications*. ACM, Warsaw, 1–5.
- [48] Wikipedia. Polydimethylsiloxane. PDMS. <https://en.wikipedia.org/wiki/Polydimethylsiloxane>.
- [49] Wikipedia. Wikipedia®. Circle contact lens. https://en.wikipedia.org/wiki/Circle_contact_lens.
- [50] Binbin Xie, Jie Xiong, Xiaojiang Chen, and Dingyi Fang. 2020. Exploring commodity rfid for contactless sub-millimeter vibration sensing. In *Proceedings of the 18th Conference on Embedded Networked Sensor Systems*. ACM, Virtual Event, Japan, 15–27.
- [51] Junli Xu, Jianliang Min, and Jianfeng Hu. 2018. Real-time eye tracking for the assessment of driver fatigue. *Healthcare technology letters* 5, 2 (2018), 54–58.

- [52] Lei Yang, Yekui Chen, Xiang-Yang Li, Chaowei Xiao, Mo Li, and Yunhao Liu. 2014. Tagoram: Real-time tracking of mobile RFID tags to high precision using COTS devices. In *Proceedings of the 20th annual international conference on Mobile computing and networking*. ACM, Maui, 237–248.
- [53] Hui-Shyong Yeo, Juyoung Lee, Woontack Woo, Hideki Koike, Aaron J Quigley, and Kai Kunze. 2021. JINSense: Repurposing Electrooculography Sensors on Smart Glass for Midair Gesture and Context Sensing. In *Extended Abstracts of the 2021 CHI Conference on Human Factors in Computing Systems*. ACM, Yokohama, 1–6.
- [54] Jintao Zhang, Jieliao Yu, Yongtao Ma, and Xiuyan Liang. 2021. RF-RES: Respiration Monitoring With COTS RFID Tags by Dopplershift. *IEEE Sensors Journal* 21, 21 (2021), 24844–24854.
- [55] Run Zhao, Dong Wang, Qian Zhang, Haonan Chen, and Anna Huang. 2018. CRH: A contactless respiration and heartbeat monitoring system with COTS RFID tags. In *2018 15th Annual IEEE International Conference on Sensing, Communication, and Networking (SECON)*. IEEE, IEEE, Hong Kong, 1–9.